Journal of Marine Research, 66, 899–925, 2008

The impact of spatial wind variations on freshwater transport by the Alaska Coastal Current

by John Rogers-Cotrone[1], Alexander E. Yankovsky[1,2,3] and Thomas J. Weingartner[4]

ABSTRACT

The Alaska Coastal Current (ACC) is located in a region with prevailing downwelling-favorable winds, flows over a long stretch of coastline (over 2000 km), and is driven by multiple sources of freshwater discharge totaling 24000 m^3 s^{-1} along its length. Using the Regional Ocean Modeling System (ROMS) we attempt to determine how spatially variable winds affect the downstream transport of freshwater along a long coastline with nearly continuous sources of freshwater. The model domain represents a fraction of the ACC region and periodic boundary conditions are applied to allow propagation of the buoyant flow from upstream. The model is forced by multiple freshwater sources in the central part of the domain and by both constant and spatially-varying, predominantly downwelling-favorable, winds. Freshwater flux gain in the coastal current (as opposed to spreading offshore) is calculated by taking a 30-day averaged difference between freshwater fluxes at the downstream and upstream edges of the buoyancy forcing region. Model runs are split into two categories: relatively high gains (50–60% of total discharge) were observed under moderate wind stress (~0.05 Pa) or no wind conditions while lower gains (35–45%) were observed under light average wind stresses (~0.025 Pa), especially when wind varied alongshore. The offshore freshwater transport is eddy-driven and is enhanced in the areas of converging wind forcing. Eddy generation is associated with the wind-induced deepening of the buoyant layer near the coast. When the surface boundary layer is thin under light wind conditions, this deepening translates into enhanced vertical shear of the alongshore current through the thermal wind balance. Reversal of alongshore wind to upwelling-favorable wind effectively blocks the downstream freshwater transport and spreads the buoyant layer offshore.

1. Introduction

The Alaska Coastal Current (ACC) as seen in Figure 1 is a wind- and buoyancy-driven coastally-trapped current that flows around the Gulf of Alaska (GOA) until it enters the Bering Sea through Unimak Pass in the Aleutian Island chain (Schumacher *et al.,* 1982). It flows year-round over a distance exceeding 2000 km (Royer, 1982; Williams *et al.,* 2007).

1. Department of Geological Sciences, University of South Carolina, Columbia, South Carolina, 29208, U.S.A.
2. Marine Science Program, University of South Carolina, Columbia, South Carolina, 29208, U.S.A.
3. Corresponding author. ***email:ayankovsky@geol.sc.edu***
4. Institute of Marine Science,University of Alaska Fairbanks, Fairbanks, Alaska, 99775, U.S.A.

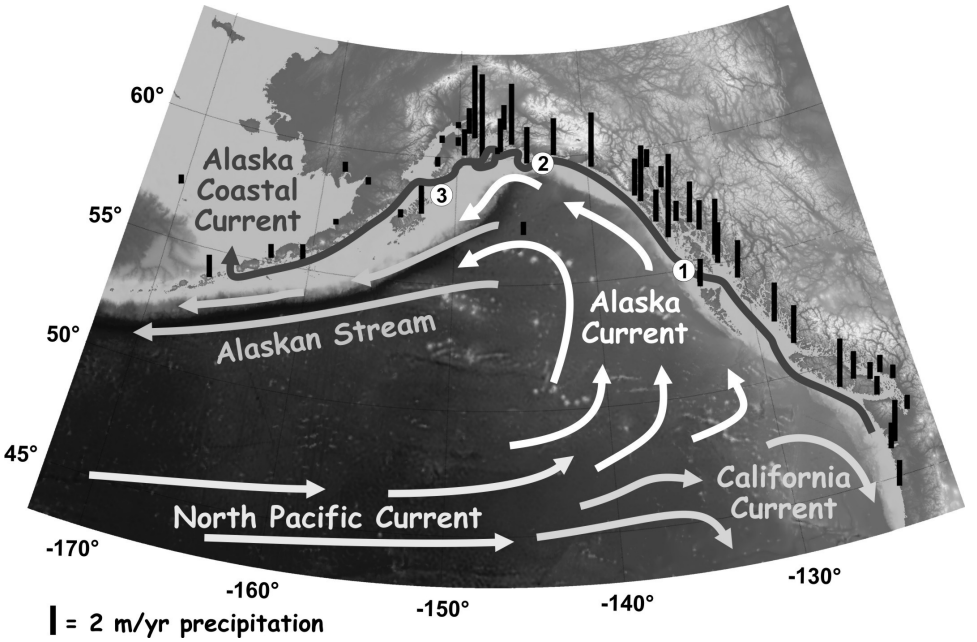

Figure 1. Map of general circulation patterns in the Gulf of Alaska. Vertical black bars show mean annual precipitation near the coast. The white circles with numbers are the QuikSCAT locations used to calculate the along-shelf wind stress time series shown in Figure 2.

The GOA shelf is subject to strong downwelling-favorable winds and a freshwater discharge with an annual average of 24,000 m^3 s^{-1} (Royer, 1982), which is delivered through numerous small rivers and streams along the entire GOA coastline. While the ACC persists year-round, seasonal variations in atmospheric forcing and freshwater inflow impact the magnitude and structure of this current.

Beginning in the fall and continuing through early spring, cyclonic winds dominate over the Gulf of Alaska and drive onshore Ekman transport and coastal downwelling. In summer these cyclonic winds weaken and intermittent upwelling events occur more frequently (Stabeno *et al.,* 2004). In conjunction with solar heating and increasing runoff, the weakened winds in summer produce a shallow upper mixed layer bounded by a strong pycnocline (Weingartner *et al.,* 2005). Throughout the year, the shelf winds exhibit considerable spatial variability. On long-term average there is more upwelling in the western and southeast Gulf than over the northern shelf (Stabeno *et al.,* 2004). On synoptic time scales, from a few days to a few weeks, the along-shelf wind stress variations can also be substantial resulting in convergent/divergent wind stress patterns (Fig. 2).

The seasonality of the discharge differs from that of the winds, with discharge at a minimum in winter when most of the precipitation is trapped on land as snow and ice and a maximum in fall when precipitation rates are also at maximum (Fig. 3). The interplay

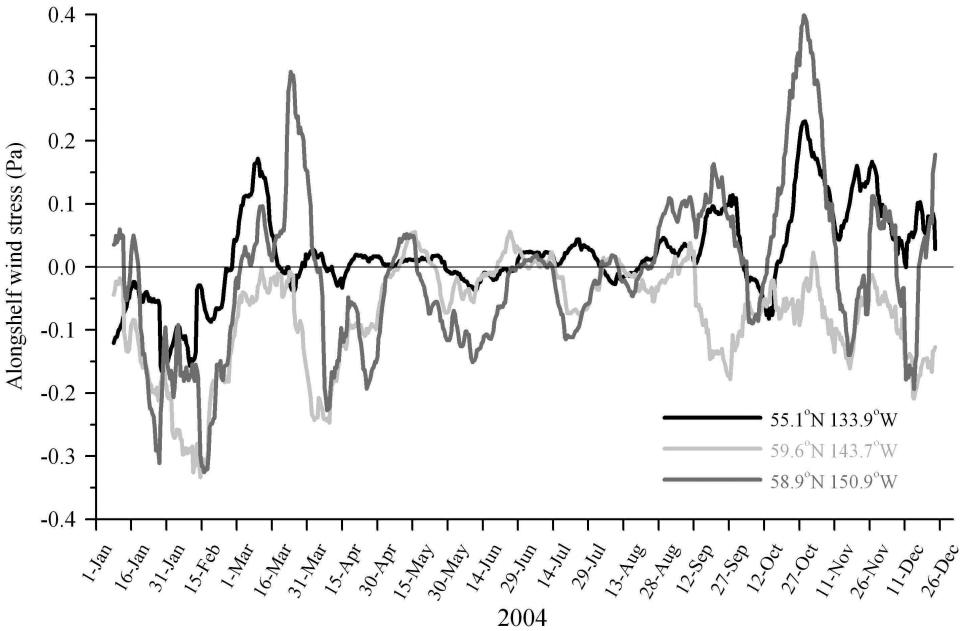

Figure 2. Time series of the along-shelf wind stress based on twice daily QuikSCAT measurements at the locations indicated in Figure 1. Each time series was smoothed with a 15-day running mean. Negative values are downwelling favorable winds and positive values are upwelling favorable winds.

between the large seasonal variations in winds and discharge give rise to similarly large seasonal variations in the dynamic structure of the ACC. Whitney and Garvine (2005) developed a "wind stress" index, to characterize a plume's along-shelf flow as either primarily wind-driven or buoyancy-influenced. The index depends upon the plume Kelvin number (Garvine, 1995), buoyant discharge rate, along-shelf wind speed, and the reduced gravity associated with the buoyant inflow and the ambient shelf water density. Upon applying their formulation to the ACC using the monthly-averaged data of Figure 3, we find that the ACC in the northern Gulf does not exceed 0.3 in the winter and is even smaller in the summer-early fall (Fig. 3). This implies that on a monthly average the ACC remains predominantly buoyancy-driven throughout the year. Nevertheless, synoptic storm events, particularly the strong winds that often occur from fall through spring, can temporarily overwhelm the buoyancy forcing.

That structure of the ACC is important to the freshwater balance of the region. The fate of ACC waters is either downstream and onto the Bering Sea shelf and eventually into the Arctic Ocean, or offshore into the Northern Pacific. The across-shelf spreading and mixing of freshwater affects the offshore location of the ACC front, stratification on the GOA shelf, and transverse and vertical circulation in the ACC. These dynamics control the

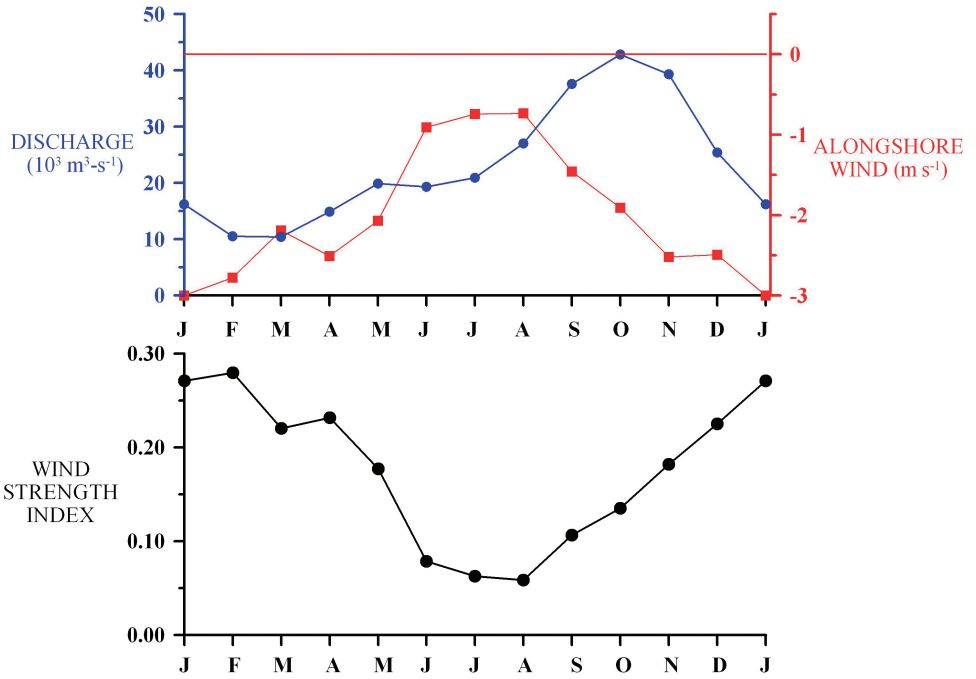

Figure 3. The mean monthly alongshore wind speed (red) and coastal freshwater discharge (blue) are shown in the upper panel. These are used to estimate the mean monthly wind stress indices (Whitney and Garvine, 2005) shown in the lower panel, with positive values imply downwelling favorable winds. The winds are based upon the ~50 year record measured at Middleton Island on the northern Gulf of Alaska (Weingartner *et al.,* 2005).

availability of micro- and macro-nutrients and influence primary production in the ACC ecosystem (Stabeno *et al.,* 2004; Weingartner *et al.,* 2005).

Previous studies of buoyancy-driven coastal currents show that buoyant discharge forms a plume composed of two dynamically distinct regions. The first is the anticyclonic bulge that forms at the mouth (or buoyancy source) with a typical width of several baroclinic Rossby radii (Garvine, 1995; Yankovsky and Chapman, 1997). The second region is a relatively narrow coastal current propagating in the Kelvin wave direction, that is, with the coast on the right in the northern hemisphere (here after we will refer to this direction as downstream). In the absence of external forcing, only a fraction of buoyant inflow continues in the downstream coastal current, while the rest accumulates in the continuously growing anticyclonic bulge (Nof and Pichevin, 2001; Fong and Geyer, 2002, Horner-Devine *et al.,* 2006).

The growth of the anticyclonic bulge can be arrested by the downstream ambient circulation (e.g., Fong and Geyer, 2002) and/or by the downwelling-favorable wind (e.g., Xing and Davies, 1999; Whitney and Garvine, 2005). Downwelling-favorable winds trap

buoyant water near the coast, steepen the isopycnals, and enhance downstream velocity in the coastal current. Upwelling-favorable winds spread buoyant water offshore, mix it with the ambient shelf water, and slow down or even reverse the coastal current (Fong and Geyer, 2001; García Berdeal *et al.,* 2002).

Buoyancy-driven coastal currents formed by multiple (or continuous) sources are an important feature of several prominent continental shelves. A few examples, in addition to the Gulf of Alaska, include the East Greenland Coastal Current which is forced by melt-water runoff from Greenland (Bacon *et al.,* 2002), the Norwegian Coastal Current (Mork, 1981) which is sustained by brackish water from fjords, and the buoyancy-driven coastal currents in the Gulf of Maine (Fong *et al.,* 1997) and in the South Atlantic Bight (Blanton and Atkinson, 1983) which are both influenced by numerous small rivers. Nevertheless, there have been only a few theoretical and/or process-oriented modeling studies of such systems published.

Narayanan and Garvine (2002) modeled a large-scale shelf circulation driven by buoyant discharge and expanded the parameter range to include cases of linear and multiple sources, but the focus of their work was the evolution of the flow field far downstream and over long time scales. Hermann and Stabeno (1996) and Stabeno and Hermann (1996) modeled the ACC using realistic discharge, wind forcing and topography. However, in their model, buoyant water ran off *upstream* from the study area with finely resolved grid, albeit through a widely distributed source. In the most relevant and recent study, Williams *et al.* (2007) applied a hierarchy of analytical and numerical models in studying the physical processes that govern ACC dynamics. They derived analytical length scales for the depth and width of the coastal current driven by a half-line source of buoyancy. The width proved to be more difficult to parameterize in the form of a simple analytical expression: after approximately 20 to 30 days, baroclinic instabilities developed in the numerical model, spreading buoyant water far beyond the offshore limit obtained in the linear analytical model. However, when downwelling-favorable wind was applied, the width stabilized because the offshore eddy flux of freshwater was opposed by onshore Ekman drift. Scaling analysis of the alongshore momentum equation that includes a wind forcing yielded a width scale for the coastal current affected by a downwelling-favorable wind. It is interesting to note that the scale worked well when the wind stress was sufficiently strong, equaling or exceeding 0.05 Pa.

This paper continues to study the effect of wind forcing on the freshwater transport in an ACC-like coastal system by means of process-oriented numerical modeling. Unlike the line source of buoyant water adopted by Williams *et al.* (2007), the freshwater is now discharged through multiple separated sources. This allows the formation of individual plumes embedded in the continuous coastal buoyancy-driven current. While uniform downwelling-favorable winds have been reasonably well studied, one aspect of the present study is on the effect of spatially variable winds. Normally buoyant plumes from single sources have spatial scales smaller than the synoptic scale in the atmosphere rendering the spatial variations in the wind field relatively unimportant. The ACC alongshore scale, on

the other hand, exceeds the typical size of the synoptic-scale atmospheric system, and spatial variations of the wind field, including along-shelf convergences and divergences, can occur over the ACC on synoptic and longer time scales (Fig. 2). In this study, we focus on the alongshore wind stress convergence/divergence which induces alongshore variations in the coastal current, sets the alongshore pressure gradient, and is potentially important for both along- and across-shelf transport of freshwater.

The rest of the paper is organized as follows: Section 2 describes the model configuration, Section 3 presents the results of numerical experiments, which is followed by the discussion of physical processes responsible for the partitioning between the offshore and alongshore freshwater fluxes under different wind conditions (Section 4), while Section 5 concludes the paper.

2. Model setup

We applied the Regional Ocean Modeling System (ROMS) to our numerical calculations (Song and Haidvogel, 1994; Shchepetkin and McWilliams, 2005). The model solves the nonlinear momentum balance and tracer (temperature/salinity) conservation equations on an *f*-plane using Boussinesq and hydrostatic approximations. Momentum advection in both the horizontal and vertical directions was approximated with a third-order, upstream-biased scheme, while tracers were advected with a third-order, upstream-biased scheme in the horizontal and a fourth-order centered differences in the vertical. Vertical turbulent viscosity and diffusivity were parameterized by the nonlocal KPP closure scheme (Large *et al.,* 1994) with a background mixing coefficient of $5 \times 10^{-6}\,\mathrm{m^2\ s^{-1}}$. The Coriolis parameter f was set to $10^{-4}\,\mathrm{s^{-1}}$.

The model domain was set as a meridionally oriented channel 80 km wide and 500 km long (Fig. 4b). The x-coordinate points offshore while the y-coordinate lies in the coastal area and points upstream. Five westernmost gridpoints were masked as a strip of coastal land with a meridional coastal wall (no normal flow) applied at $x = 5$ km. This coastal area was cut through by ten zonal inlets delivering buoyant water into the domain (see below). The GOA shelf differs from most oceanic shelves in that its depth drops steeply from the coast to ~150–200 m and then remains fairly uniform over the whole shelf width. The model bottom topography mimics this feature and slopes linearly from a depth of 5 m near the coast ($x = 6.875$ km) to a depth of 200 m over a horizontal distance of 10 km with a constant depth farther offshore (Fig. 4a). Horizontal resolution is 1.25 km in the x-direction and 2.5 km in the y-direction. 25 layers were applied in the vertical s-coordinate with the finest resolution occurring in the surface and bottom boundary layers (Fig. 4a). The baroclinic time step for all runs was 120 seconds and the barotropic time step was 6 seconds.

The following boundary conditions were applied: eastern and western walls were slippery, and a quadratic bottom friction with a drag coefficient of 3×10^{-3} was specified at the bottom. The freshwater entered the domain through ten inlets placed at 25 km apart in the middle of the coastal strip (hereafter referred to as "the source region"). The

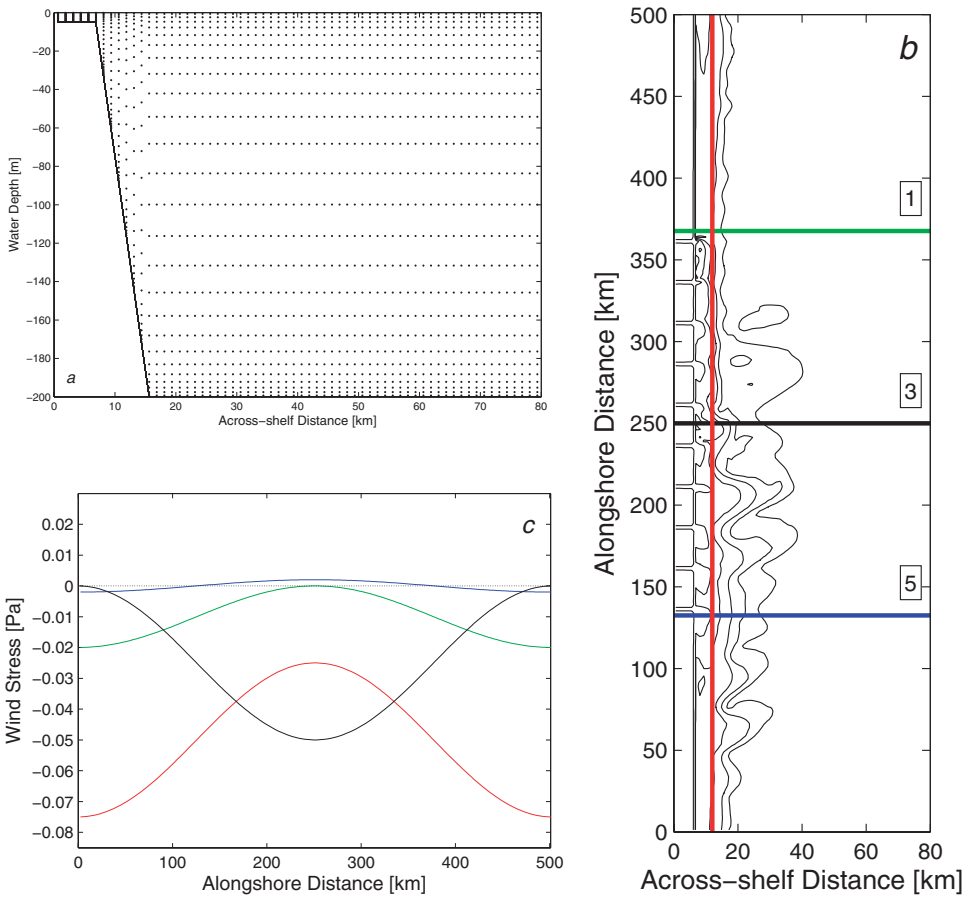

Figure 4. Model configuration: (a) across-shelf transect showing the vertical grid spacing, heavy line is bottom; (b) plan view of the model domain showing locations of vertical transects for the freshwater flux calculations and salinity contours (22:2:30) at day 20, Case G; (c) alongshore variations of wind stress, Cases H (red), O(green), N (blue), and L (black).

freshwater (zero salinity) discharge was prescribed with a constant rate of 200 $m^3\ s^{-1}$ at the head of each inlet ($x = 0$ km). The inflow was partially mixed with the ambient water forming a vertical density and velocity structure by the time it progressed through the mouth. This boundary condition is preferable compared to the artificially prescribed constant inflow at the mouth with fixed salinity/density anomaly (Yankovsky, 2000).

a. Periodic boundary conditions

The major focus of this study is to determine how wind will affect the structure of a buoyant flow originating from multiple sources. This requires that our model domain be subjected to inflow from upstream coastal sources of freshwater (remote buoyancy

forcing). Indeed, the continuity of the ACC system can be traced as far upstream as British Columbia or even the Washington Coast if conditions are favorable (i.e., the Columbia River discharge) as suggested in Figure 1 and by Royer (1982). In order to best approximate a continuous flow like the ACC with multiple coastal sources as well as input from upstream, to maintain a sufficient horizontal resolution (less than the baroclinic Rossby radius), and to minimize computational requirements, our domain is only a fraction of the size of the actual ACC. Hence we introduced periodic boundary conditions so that water flowing through the downstream open boundary ($y = 0$ km) re-enters the domain at the upstream boundary ($y = 500$ km) and mimics the upstream portion of freshwater input found in any segment of the GOA shelf. Figure 4b is an example of the resulting salinity field. This set-up has an advantage over simply introducing a constant flow at the upstream boundary as has been done in previous studies. It assures that the flow from upstream has the structure of a buoyancy-driven coastal current. Periodic boundary conditions lead to a continuous increase of freshwater content in a recirculating coastal current, which can be viewed as a drawback and complicates the interpretation of model results. However, this situation is not unrealistic as it corresponds to the increase in coastal freshwater discharge during summer and early fall in the ACC region.

b. Wind forcing

Three major patterns of wind forcing were used: no wind, constant wind, and spatially variable wind. In the constant wind cases, a downwelling-favorable wind stress was applied with four different values: -0.1 Pa, -0.075 Pa, -0.05 Pa, and -0.025 Pa. These values cover a typical range of monthly-averaged wind stress variations over an annual cycle in the GOA region. In the variable wind cases, only alongshore (y-direction) variations were considered. Two different spatially-variable wind patterns were introduced. One had the strongest wind stress at the upstream/downstream edges of the model domain and the lowest wind stress in the center ($y = 250$ km). The second had the reversed structure: the lowest wind stress at the upstream/downstream edges and the strongest wind stress in the center. Wind stress varied in the alongshore direction as one period of a harmonic function. This arrangement ensures that wind stresses at the upstream and downstream edges of the domain were equivalent; a necessary condition given the periodic boundary conditions of our model. Each pattern of variable wind stress is then characterized by a mean wind stress (averaged over the entire length of the domain) as well as local extreme values located at the center of the model domain and at its edges. For example, the wind stress pattern $\tau(y)$ shown in Figure 4c (red line) has the strongest wind stress at the edges (-0.075 Pa), the lowest wind stress in the center (-0.025 Pa), and an average wind stress of -0.05 Pa:

$$\tau(y) = T(0.5 + 0.25 \cos(2\pi y/L)), \tag{1}$$

where T is the scaling factor representing the maximum wind stress magnitude in our model runs ($T = 0.1$ Pa) and L is the length of the model domain.

c. Initial conditions

The model runs began with water initially at rest. Ambient salinity was set at 32 (Practical Salinity Scale) and water temperature was set at 4°C, with a corresponding density anomaly of 25.3 kg m^{-3}. The wind forcing and freshwater input were turned on at the initial time step and the model evolved for a period of 50 days.

3. Model results

The partitioning of freshwater discharge between offshore and alongshore components was determined by calculating a freshwater flux through several across-shelf transects spanning the entire width of the model domain. The transects were placed upstream, in the middle, and downstream of the source region (marked as 1, 3, and 5, respectively, in Fig. 4b). The freshwater flux F through these transects is defined as:

$$\mathcal{F} = \int_{-h}^{\eta} \int_{0}^{W} v \frac{s_0 - s}{s_0} \, dz dx, \tag{2}$$

where η is the sea-surface height, h the is water depth, W is the channel width, v is the alongshore velocity component, $s_0 = 32$ is the background salinity, and s is the salinity. Negative values of flux correspond to freshwater moving in the downstream direction. Additionally, in several model runs a fourth, alongshore transect (red line in Fig. 4b) was used to calculate offshore freshwater flux. This fourth transect was placed at various distances offshore depending upon the structure of the plume.

a. No wind and constant wind cases

First, we consider two model runs, without the wind forcing (Case A, Table 1) and with a constant wind stress of -0.075 Pa (Case B). These examples will help to delineate the formation of a continuous buoyancy-driven current and the effects of constant wind stress. From Figure 5a and b it is clear that the horizontal density structure of the two buoyancy-driven currents developed by day 40 is quite different. Without wind, freshwater spreads significantly farther offshore than it does under constant downwelling-favorable wind. Comparison of vertical transects (Fig. 6a and b) shows that the wind not only traps the buoyant water inshore, but also deepens the buoyant layer. In Case A (Fig. 6a), the buoyant layer (defined here by the 25 kg m^{-3} isopycnal) extends more than 25 km offshore and occupies the upper 20 m of the water column. In this case, the isopycnals are nearly horizontal and the plume is of the surface-advected type (Yankovsky and Chapman, 1997). In the presence of wind (Fig. 6b), the buoyant layer penetrates deeper (down to 40 m) and the isopycnal slopes are much steeper, extending only 7–8 km from the coast. The downstream jet in Case A has a typical along-shelf velocity of -0.2 to -0.4 m s^{-1}. Below the buoyant layer, a countercurrent exceeding 0.05 m s^{-1} forms. This flow pattern resembles a lateral estuary, since the countercurrent compensates for continuous entrain-

Table 1. Freshwater flux gain and wind forcing in model cases. Wind: C—constant, V—variable; wind range (for variable wind only): first number is the wind stress at the edges of model domain, second number is the wind stress in the center.

Case	Wind	Wind Range, Pa	Avg. Wind, Pa	Gain, $m^3\ s^{-1}$
A	None	—	0	1210
B	C	—	−0.075	1210
C	C	—	−0.1	1170
D	V	−0.025, −0.075	−0.05	1130
E	C	—	−0.05	1130
F	V	−0.1, −0.05	−0.075	1110
G	V	−0.05, 0	−0.025	1100
H	V	−0.075, −0.025	−0.05	1090
I	V	0, −0.1	−0.05	1090
J	V	−0.1, 0	−0.05	1020
K	C	—	−0.025	849
L	V	0, −0.02	−0.01	823
M	V	0, −0.05	−0.025	801
N	V	−0.002, 0.002	0	797
O	V	−0.02, 0	−0.01	692

ment and downstream transport of ambient water being mixed with the coastal current. Wind forcing (Case B) enhances (~ -1 m s^{-1}) and deepens (>80 m) the downstream coastal jet, and also hinders the development of a countercurrent.

The large offshore excursions of freshwater observed in the structure of the flow in Figure 5a are relics from an adjustment period early in the model run when the anticyclonic bulges, in the absence of an ambient downstream flow, were free to grow and spread offshore. Once the flow from upstream began to affect the source region, bulge growth was arrested while the remnants from early in the model run remained. This scenario is confirmed by analyzing the freshwater fluxes.

We used daily averaged values of velocity and salinity to compute the along-shelf freshwater flux time series over the 50-day period for each model run through the three across-shelf transects. The time series were further smoothed by passing through a 5-point filter:

$$\hat{\varphi}_i = 0.44\varphi_i + 0.23\varphi_{i\pm1} + 0.05\varphi_{i\pm2},$$

where φ_i is the i^{th} element of the velocity/salinity daily averaged time series.

Overall, the freshwater fluxes grow faster in Case B than in Case A, although the buoyancy-driven current is forced by the same freshwater discharge in both cases (Fig. 7a, b). This difference is due to the influence of downwelling-favorable wind stress, which deepens and accelerates the coastal jet. In the early stages of the model runs (0–5 days), the freshwater fluxes grow only at the central and downstream transects, while remaining zero

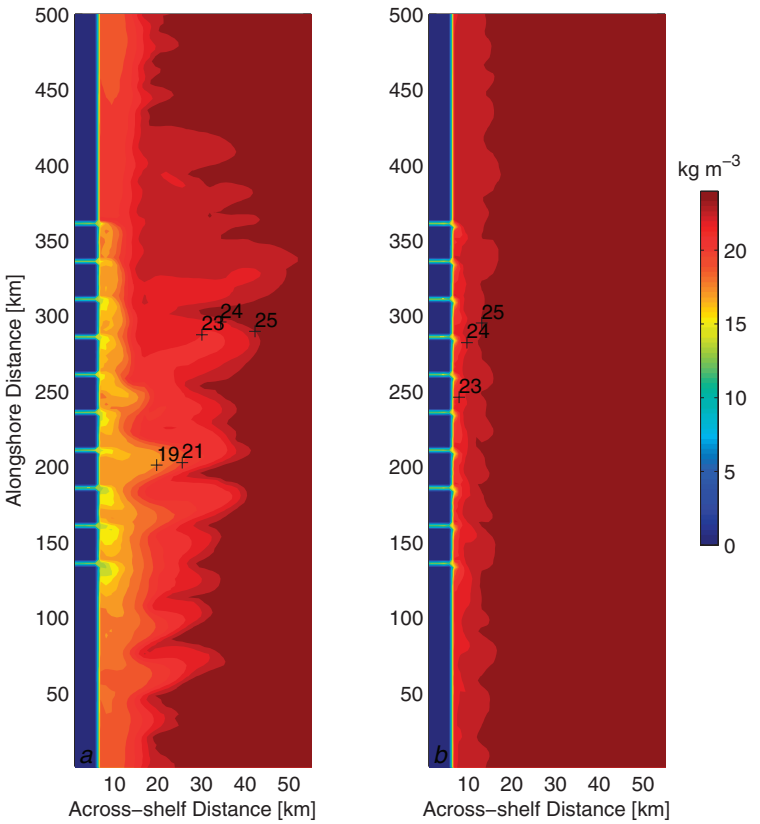

Figure 5. Plan view of density field at the surface on day 40, Case A (a) and Case B (b).

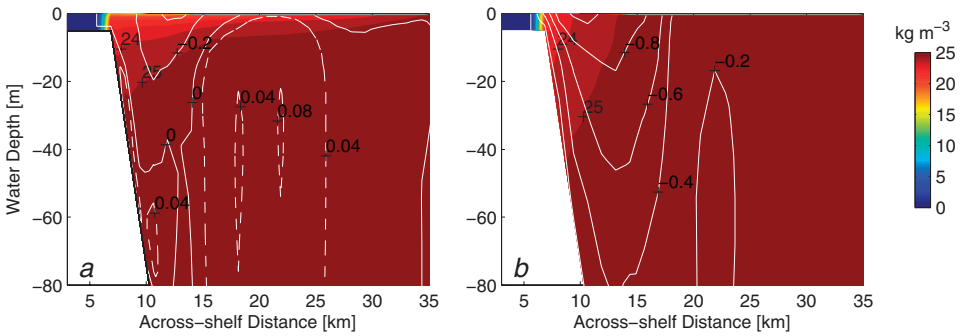

Figure 6. Across-shelf sections of density (shading) and alongshore velocity (contours) on day 40, Transect 3 for Case A (a), and Case B (b).

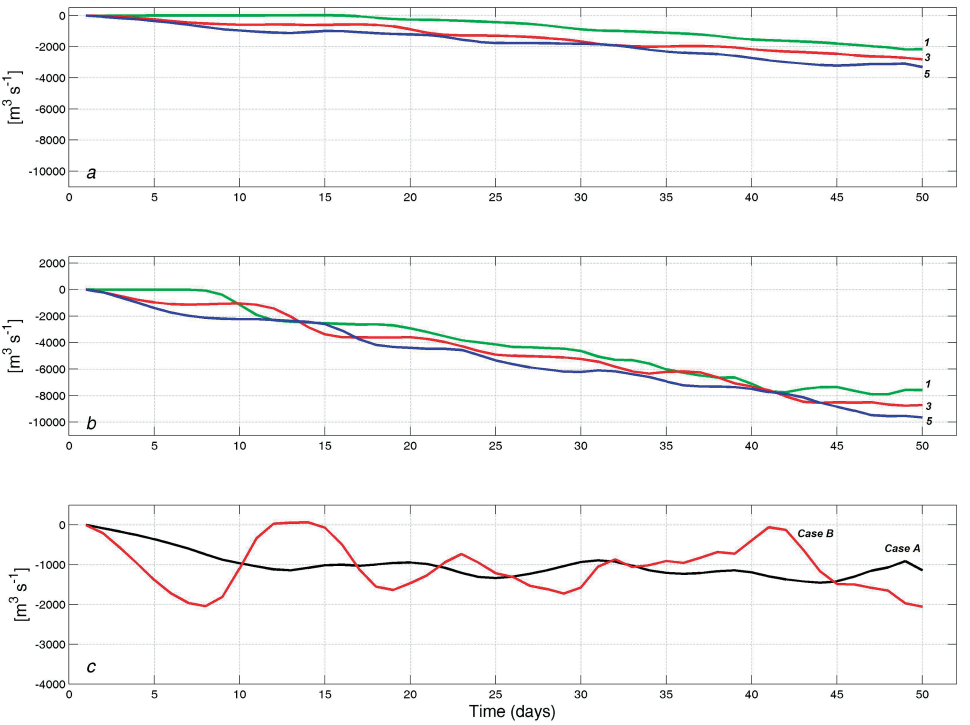

Figure 7. Alongshore freshwater flux at Transect 1 (green), Transect 3 (red), and Transect 5 (blue) for (a) Case A, (b) Case B, and (c) the difference between freshwater fluxes at Transects 5 and 1 (freshwater flux gain) for Case A (black) and B (red).

upstream (since there is no freshwater yet coming from upstream). In Case B the freshwater flux reaches a constant value at Transect 5 (downstream) by day 7 (Fig. 7b), and its magnitude is exactly the same as the freshwater discharge into the domain through the source region, 2000 $m^3\ s^{-1}$. A freshwater flux at transect 5 in Case A stops growing after 10 days (Fig. 7a), but its maximum value is only a fraction ($\sim$1100 $m^3\ s^{-1}$) of the freshwater discharge into the domain. The rest of the discharge is accumulated in continuously growing bulges. The establishment of the continuous buoyant flow occurs after freshwater passes through the periodic boundary, emerges from the upstream edge of the model domain, and arrives at the source region. At this point the freshwater flux starts to grow at Transect 1 as well (on day 8 in Case B and approximately on day 16 in Case A). After the buoyancy driven current has closed the loop, the freshwater flux grows at all three transects, but at a higher rate under wind forcing (Case B).

In the model of the buoyancy-driven coastal current originating from a single source of freshwater, the fate of discharge in the coastal current can be traced by comparing the freshwater discharge with the freshwater flux through some downstream transect (i.e., Fong and Geyer, 2002). In our model configuration, the freshwater flux carried by the

coastal current through the downstream transect 5 is affected (i) by the freshwater inflow in the source region, and (ii) by the continuously growing freshwater flux through the upstream transect 1. In order to delineate the fate of a local (source region) discharge, we take the difference between the freshwater fluxes through transects 5 and 1, and refer to this quantity as the ***gain*** of along-shelf freshwater flux through the source region. Unlike the freshwater flux, its gain does not steadily increase with time but fluctuates around some average value. The gain should equal 2000 m^3 s^{-1} or the total discharge from the freshwater sources in the source region if all of that discharge is transported downstream (i.e., if the buoyant layer does not spread offshore). However, this situation is unlikely to occur because the newly discharged freshwater causes a lateral spreading of the buoyant layer and a consequent reduction of the gain. Furthermore, freshwater can be lost offshore due to the mixing processes between buoyant and ambient waters. Values of gain less than 2000 m^3 s^{-1} imply that freshwater discharge is partitioned between downstream and offshore fluxes. Figure 7c shows the temporal evolution of freshwater flux gain for Case A vs. Case B. Two surprising results arise: (i) on average, freshwater flux gain under downwelling-favorable wind stress does not exceed the gain in the case of no wind forcing, especially after the continuous buoyancy-driven current has been established (after day 15); (ii) the gain exhibits much stronger temporal fluctuations in the presence of stationary wind forcing compared to no-wind conditions.

The freshwater flux gain was then averaged over a 30-day period, from day 20 through day 50. This averaged value was used as an overall characteristic of freshwater fate in each model run and starting from day 20 allowed sufficient time to develop a continuous (re-circulating) buoyancy-driven current in the domain. As mentioned earlier, it took ~15 days for the buoyancy-driven current to "return" to the source region through the upstream boundary in the absence of wind forcing, and this time interval was shorter under downwelling-favorable wind conditions.

The upper limit for the freshwater flux gain G under conditions of a continuously growing freshwater flux from the upstream can be scaled as follows. The derivation closely follows previous studies by Yankovsky and Chapman (1997) and Lentz and Helfrich (2002). We assume that the coastal current in the source region is forced by a freshwater flux F at the upstream edge (through transect 1 in Fig. 4b) and by multiple sources of freshwater through the coastline which when combined equal the total freshwater inflow I. Subsequently, the buoyant layer entrains the ambient water (but no freshwater is lost from the coastal current) so that the density anomaly ρ' is less than the density anomaly ρ'_0 of freshwater relative to the ambient water. The buoyancy fluxes from the upstream Q_u and from the coastal sources Q_i are then defined as:

$$Q_u = \mathcal{F}\,\frac{\rho'_0}{\rho'} \qquad Q_i = \mathcal{I}\,\frac{\rho'_0}{\rho'}. \tag{3}$$

The buoyant layer maintains contact with the bottom to the maximum depth h_b

$$h_b = (2Qf/g')^{1/2}, \tag{4}$$

where Q is the buoyancy flux, g' is the reduced gravity: $g' = g\rho'/\rho_0$, and ρ_0 is the ambient water density. At the h_b isobath, the buoyant layer detaches from the bottom and outcrops offshore over a horizontal distance of a baroclinic Rossby radius Rd

$$Rd = (g'h_b)^{1/2}/f. \tag{5}$$

Assuming a linear depth profile, the total cross-shelf area A occupied by a coastal current is

$$A = \frac{1}{2}\left(\frac{h_b^2}{\alpha} + h_b Rd\right), \tag{6}$$

where α is the bottom slope. For the upstream and downstream boundaries of the source region (transects 1 and 5 in Figure 4b, respectively), $A_1 = A(Q_u)$ and $A_5 = A(Q_u + Q_i)$. The increase of the across-shelf area in the buoyancy-driven coastal current at the downstream location requires the buoyant discharge at the source region to fill this extra volume V of the coastal current:

$$V = \frac{1}{2}\Delta A L_s, \tag{7}$$

where $\Delta A = A_5 - A_1$ and L_s is the length of source region. This lateral expansion occurs over a characteristic time $t = L_s/u$, where u is the average speed of the coastal current, so that $V = aQ_iL_s/u$, where a is the fraction of buoyant inflow which is spent on the offshore expansion. Equating two expressions for V yields the freshwater flux gain G as a percentage of the coastal buoyant inflow:

$$\mathcal{G} = (1 - a)100\% = \left(1 - \frac{1}{2}\frac{\Delta A u}{Q_i}\right)100\%. \tag{8}$$

The along-shelf speed can be scaled by using geostrophic across-shelf momentum balance:

$$u = \frac{g'}{f}\frac{h_b}{Rd} \approx \overline{(g'h_b)^{1/2}}, \tag{9}$$

where overbar denotes an average between the values at the upstream (transect 1) and the downstream (transect 5) edges of the source region.

We estimate the freshwater flux gain for a coastal current with typical characteristics of freshwater flux and density anomaly obtained in the numerical experiments by following the equations (3)–(6), (9) and (8). Figure 8 illustrates how G depends on the density anomaly of the coastal current (a) and on the freshwater flux from the upstream (b) assuming the following values representative of our model experiments: $\rho_0 = 1025$ kg m^{-3}, $\rho' = 5$ kg m^{-3} in Figure 8b and variable in Figure 8a, $\rho_0' = 25$ kg m^{-3}, $F = 2000$ m^3 s^{-1} in Figure 8a and variable in Figure 8b, $I = 2000$ m^3 s^{-1}, $\alpha = 0.02$.

For a density anomaly varying in the range of 4–10 kg m^{-3}, the freshwater flux gain is remarkably stable and is close to 60% (Fig. 8a). This gain is similar to that obtained over

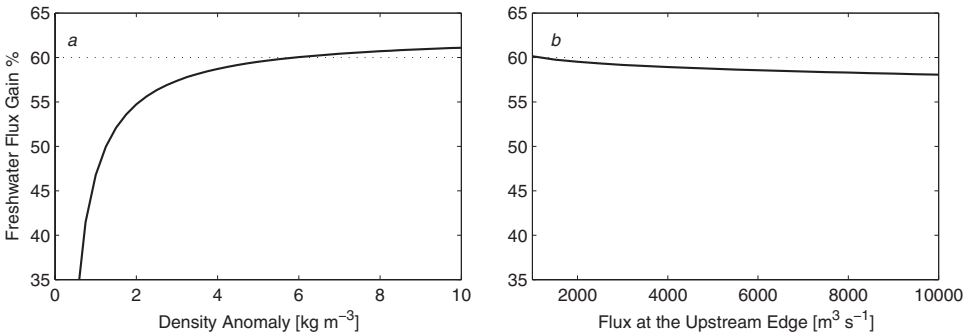

Figure 8. Estimation of freshwater flux gain based on the equations (3)–(9): freshwater flux from the upstream $F = 2000$ m^3 s^{-1} (a) and density anomaly $\rho' = 5$ kg m^{-3} (b).

the 30-day averaging period of case A (Table 1), where the density anomaly of the coastal current exceeded 5 kg m^{-3} within the source region (Fig. 5a). The gain shows a weak dependence on the volume of the buoyancy flux coming from upstream (within the specified range of Q_u), and slightly decreases with the increase of Q_u (Fig. 8b). It should be noted that the derivation (3)–(9) intrinsically assumes that the current from upstream is strong enough to suppress the growth of anticyclonic bulges, and so the curve in Figure 8b can not be continued to very low values of Q_u. The gain can exceed the upper limit of 60% under strong downwelling-favorable wind forcing, when the newly discharged buoyant water is advected downstream faster than it spreads and adjusts laterally. However, these regimes are beyond the scope of this paper and were not attained in our model experiments.

All model runs are summarized in Table 1 and Figure 9, with the latter being a more visual way of presenting the information in the table. The model runs in the table are arranged in descending order with respect to their 30-day averaged gain. If variable wind stress is present, it is characterized by three values: average stress (shown as green diamonds in Fig. 9), stress at the edges of model domain (red circles, Fig. 9), and stress in the center of source region (blue triangles, Fig. 9).

In all model runs the freshwater flux gain never exceeded 60% of the freshwater discharge in the source region (which was 2000 m^3 s^{-1}), consistent with our scaling arguments. Model runs were split into two groups with most of the runs having a gain between 1000 and 1200 m^3 s^{-1} (50–60% of the discharge). This group includes a model run with no wind, all runs with constant wind stress (except for the weakest constant wind stress of -0.025 Pa), and all variable wind runs with an average of -0.05 Pa wind stress or greater. The second group has gains ranging from 700 to 900 m^3 s^{-1} (35–45% of the discharge). This group includes all runs with average wind stress between 0 and -0.025 Pa. It also includes one run where wind stress reversed to upwelling-favorable in the center of the domain going from -0.002 Pa on the boundaries to $+0.002$ Pa in the center (Case N).

An important result is the substantial decrease in gain when light winds, whether constant or spatially-variable, force the model. The focus of this study, therefore, is on the

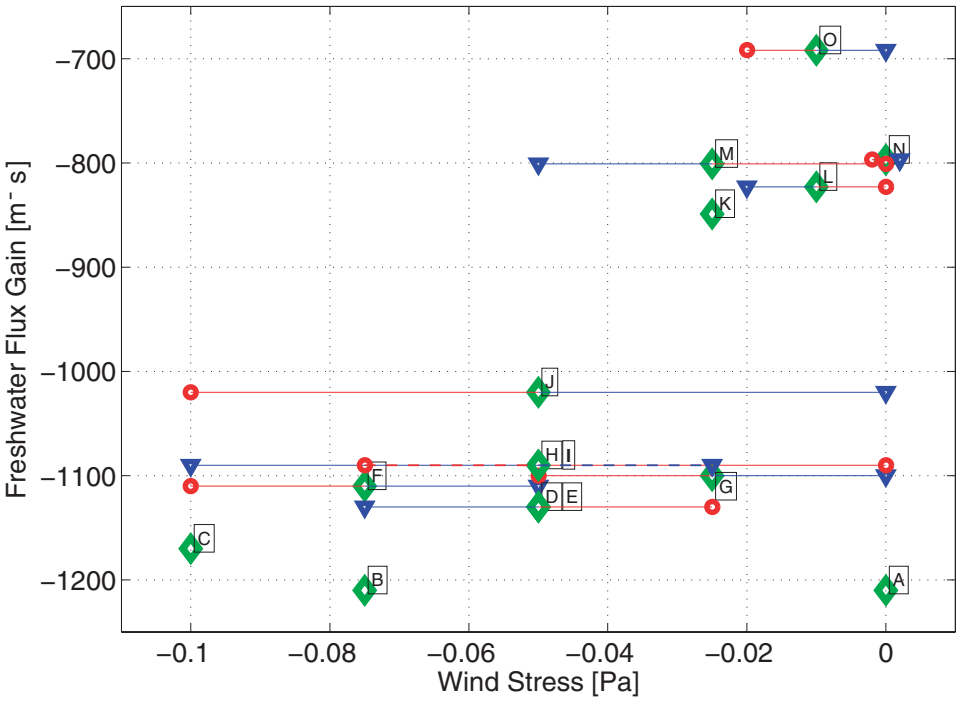

Figure 9. Freshwater flux gain versus wind stress in all model cases presented (marked with letters): the average wind stress is shown as a green diamond, a blue triangle is the wind stress in the center of model domain, and a red circle is the wind stress at the edges of model domain. Note the same gain in cases H and I as well as D and E.

effects that light and spatially-varying winds have on the structure of a buoyancy-driven current. For the moment it is apparent that under such conditions some freshwater is lost from the coastal current.

First, we analyze the effects of spatially uniform wind. Comparison of no wind vs. constant wind stress model runs (Cases A and B) shows that the freshwater flux and its gain exhibit strong fluctuations on a temporal scale of several days under the influence of downwelling-favorable wind. We infer that this results from the development of instabilities, which modulate the downstream freshwater transport and also set the offshore eddy-driven freshwater flux. The instabilities of frontal jets are often related with the vertical shear of the along-front velocity component, that is, eddy driven flux is caused by the across-front density gradient through the thermal wind shear (e.g., Gill, 1982). Using this relationship, Spall and Chapman (1998) parameterized the across-front eddy density flux as a function of the across-front density difference. Since a downwelling-favorable wind stress steepens the isopycnals (Fig. 6b), it can also trigger the development of instabilities.

Figure 10 compares time-averaged vertical profiles of the vertical shear of the *v*-

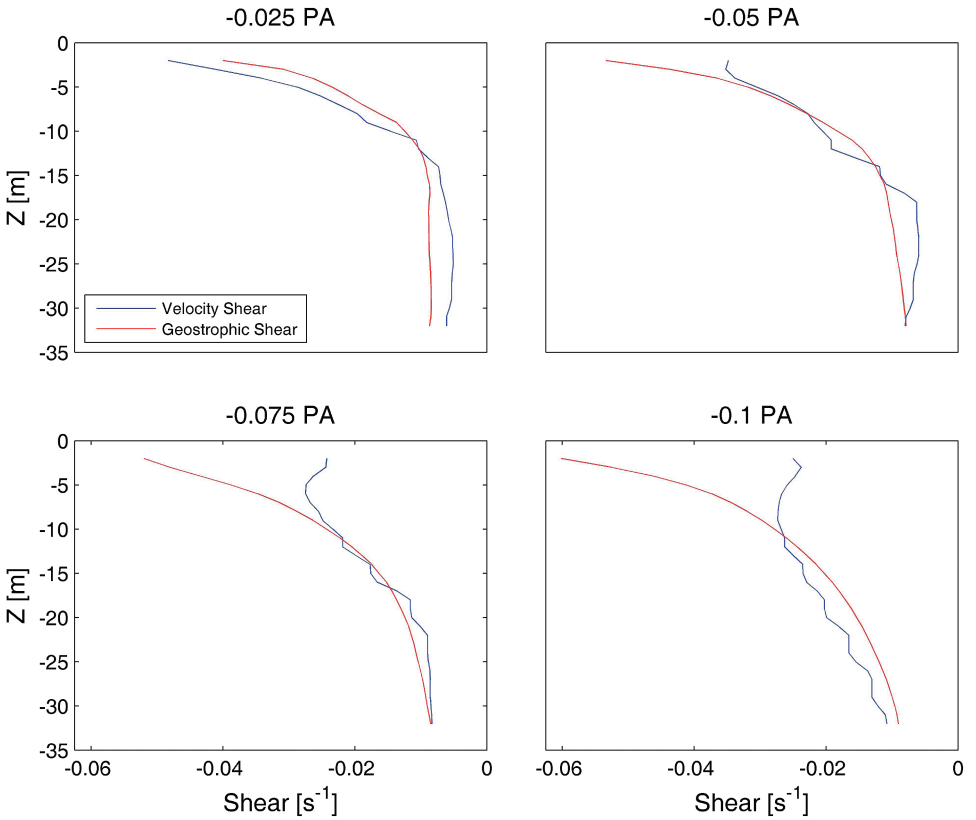

Figure 10. 10-day averaged vertical shear of alongshore velocity, modeled (blue) and geostrophic (red), at Transect 3 for cases with constant wind stress: K (−0.025 Pa), E (−0.05 Pa), B (−0.075 Pa), and C (−0.1 Pa).

(alongshore) component, both geostrophic and actual, in the center of the source region for the four cases with constant wind. The estimates were obtained as follows: for each daily averaged across-shelf transect (days 36 through 45) at $y = 250$ km (Transect 3, Fig. 4b) the vertical profile with maximum geostrophic (thermal wind) shear was determined. The vertical profile of the actual vertical shear for the v-component at the same offshore location was also calculated. These profiles were then averaged over a 10-day period. In most cases, the maximum geostrophic shear at Transect 3 occurred ~4 km offshore. Four model runs with constant wind stresses (Cases B, C, E, and K) suggest that the strongest offshore eddy flux develops in Case K (wind stress −0.025 Pa) with the lowest downstream freshwater flux gain of ~850 $m^3\ s^{-1}$. As expected, the geostrophic shear progressively grows with the magnitude of the wind stress (from Case K through Case C—Fig. 10). However, the actual shear at the same location (responsible for the generation of instabilities) decreases with the strengthening wind stress.

This tendency can be explained as follows. The onshore Ekman drift tilts the isopycnals at the coast. This process generates the available potential energy (APE) in the coastal current at the rate proportional to the wind stress and consequently to the wind speed squared: $APE \propto W^2$. The APE generation then translates into the vertical geostrophic shear. At the same time the wind forcing induces turbulent stresses in the surface boundary layer which offset the geostrophic balance. The rate of dissipation of turbulent kinetic energy ε is $\varepsilon \propto u_*^3 \propto W^3$, where u_* is the friction velocity. Hence, the turbulent viscosity grows at a faster rate as a function of wind speed than the geostrophic vertical shear. As a result, the actual vertical shear departs from the gesostrophic shear and diminishes in the surface layer (5–10 m deep) as the wind stress becomes stronger (Fig. 10). For example, under the wind forcing of -0.1 Pa the actual vertical shear magnitude in the upper 10-m layer is $\sim 0.025\ s^{-1}$, while the goeostrophic shear continuously grows towards the surface to unrealistically high value of $0.06\ s^{-1}$. The corresponding Ekman transport U_E in this case is $U_E = \tau/\rho f \sim 1\ m^2\ s^{-1}$. If we assume that U_E is confined within the upper 10 m (as Figure 10 suggests) and that the velocity changes as a linear function in vertical, this will yield a wind-induced vertical shear of $\sim 0.02\ s^{-1}$, which is close to the actual value.

This implies that the light wind produces the strongest vertical shear in the frontal jet (close to the geostrophic), which translates into the strongest offshore eddy flux of freshwater. Also, as the wind stress increases, the offshore eddy flux is opposed by progressively increasing onshore Ekman transport, which further limits the offshore expansion of freshwater.

b. Spatially variable winds

Downstream freshwater flux gain is further reduced when light downwelling-favorable wind has spatial variations (i.e., Cases L, M, O—see Fig. 9 and Table 1). We will analyze two model runs with the lowest gains, Cases M and O. The wind stress variations in these cases have opposite patterns: wind stress magnitude is a maximum in the center of the source region and subsides at the edges of the model domain in Case M, while it has a maximum magnitude at the edges and is zero in the middle of the source region in Case O.

Case M is summarized in Figure 11. The 30-day averaged alongshore freshwater transport (product of an alongshore velocity component and a relative salinity anomaly under the integral in (2)) through transects 1 and 5 is shown in Figures 11a and 11b, respectively; and the gain between these two transects is in Figure 11c. Freshwater is transported in the upper 30-m of the water column and lies within 10–15 km off the coast. The gain in freshwater transport through the source region occurs within 8 km off the coast (negative numbers in Fig. 11c), while farther offshore, the gain changes sign, that is, the downstream freshwater transport decreases. Since both transects are affected by the same wind stress, this decrease cannot be attributed to the onshore shift of the buoyancy-driven current by the downwelling-favorable wind. We infer that the decrease of freshwater transport at the offshore flank of the coastal current is likely due to the loss of buoyant water offshore.

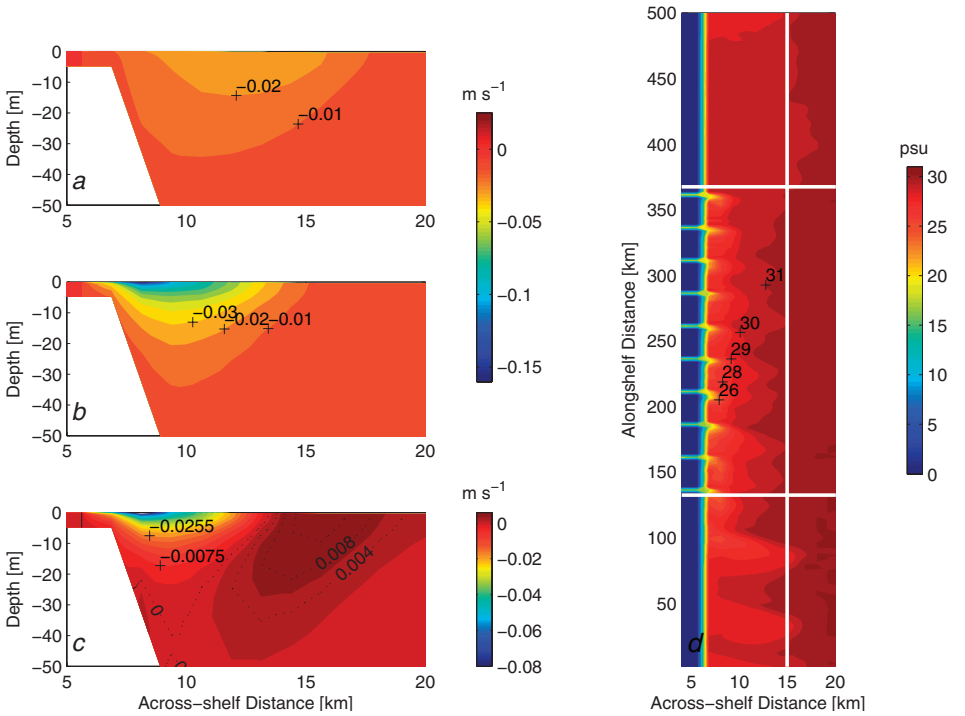

Figure 11. Model case M: 30-day averaged freshwater transport through transect 1 (a), transect 5 (b), its gain between transects 1 and 5 (c), and plan view of salinity field at the surface on day 40.

For case O, the 30-day averaged freshwater transport at transects 1 and 5 (Fig. 12a and b) occurs in a shallower (e.g., 20-m deep) layer and extends further offshore compared to Case M. The offshore extension of the buoyant layer is maximal in the source region (Fig. 12d) and contracts at the edges of model domain, where the wind stress is stronger, which is opposite to the Case M pattern. The gain of freshwater transport is concentrated in the upper 10-m layer, and freshwater loss occurs in the intermediate layer (10–30 m deep). In comparing Figures 11c and 12c, the difference between Cases O and M is the location of the region where downstream freshwater transport decreases. In Case M this area is on the offshore side of the plume while in Case O it is beneath it.

Both Case O and Case M have a gain of substantially less than 50% of the input from the coast. The different structures of the plumes (see the plan views in Fig. 11d and 12d) as well as the structure of the downstream freshwater gain in the vertical across-shelf transects suggests that in these cases the offshore loss of freshwater occurs through different pathways.

Further insight into the offshore transport mechanism is obtained upon comparing the 30-day averaged offshore freshwater transport and its integral, freshwater flux, through the

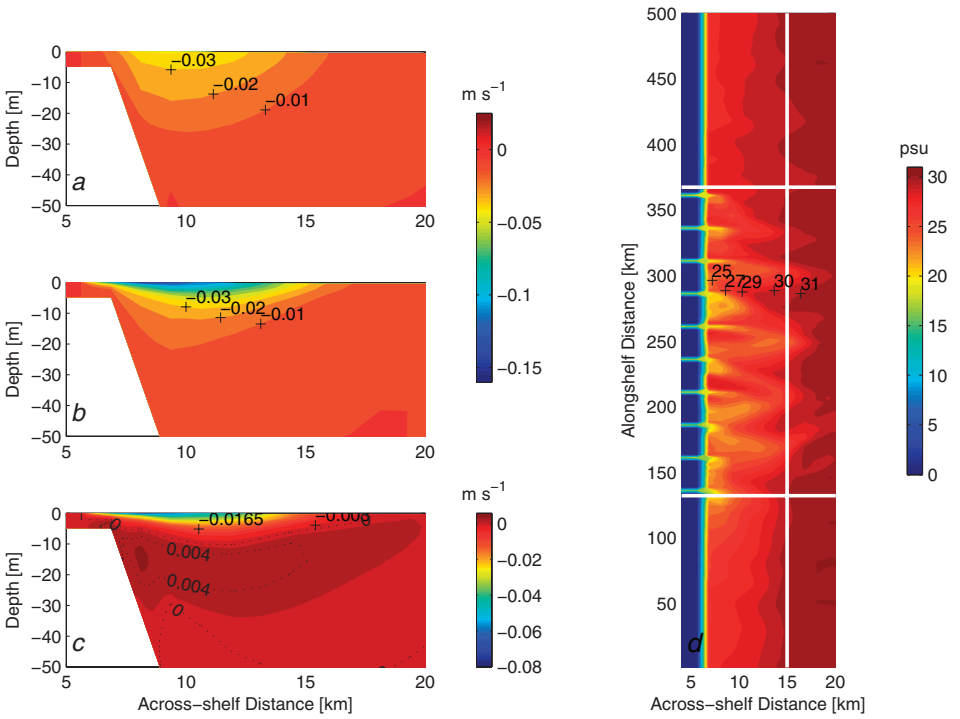

Figure 12. Same as Figure 11 but for model case O.

transect along the entire model domain (i.e., vertical white lines in Fig. 11d, 12d). The total freshwater transport is partitioned into two components, a mean and an eddy transport:

$$\left\langle u\,\frac{s_0 - s}{s_0}\right\rangle = \langle u\rangle\left\langle\frac{s_0 - s}{s_0}\right\rangle - \left\langle u'\,\frac{s'}{s_0}\right\rangle. \tag{10}$$

Here $\langle \ldots \rangle$ refers to a 30-day averaging, and variables with primes represent fluctuations about the corresponding mean values. As "instantaneous," we use daily averaged salinity and velocity fields (similar to the alongshore freshwater flux calculations).

Integrating (10) with respect to alongshore and vertical coordinates yields the offshore freshwater flux. Total, mean, and eddy fluxes as functions of the across-shelf coordinate are shown in Figure 13 (cases M and O). In both cases, the total offshore flux decays offshore, faster in Case M (with stronger average wind). The mean freshwater flux becomes negative at $x \sim 9$ km (Case M) and $x \sim 11$ km (Case O), fairly close to the coast (only 4–6 km off the coastal wall at $x = 5$ km) and reaches its minimum value of ~ -1000 m^3 s^{-1} at $x \sim$ 15–17 km. This mean onshore freshwater flux is primarily sustained by the onshore Ekman transport (see below). The eddy flux remains positive within 20 km from the coast, and its maximum value is larger in Case O ($\sim$1200 m^3 s^{-1}) than in Case M ($\sim$750 m^3 s^{-1}).

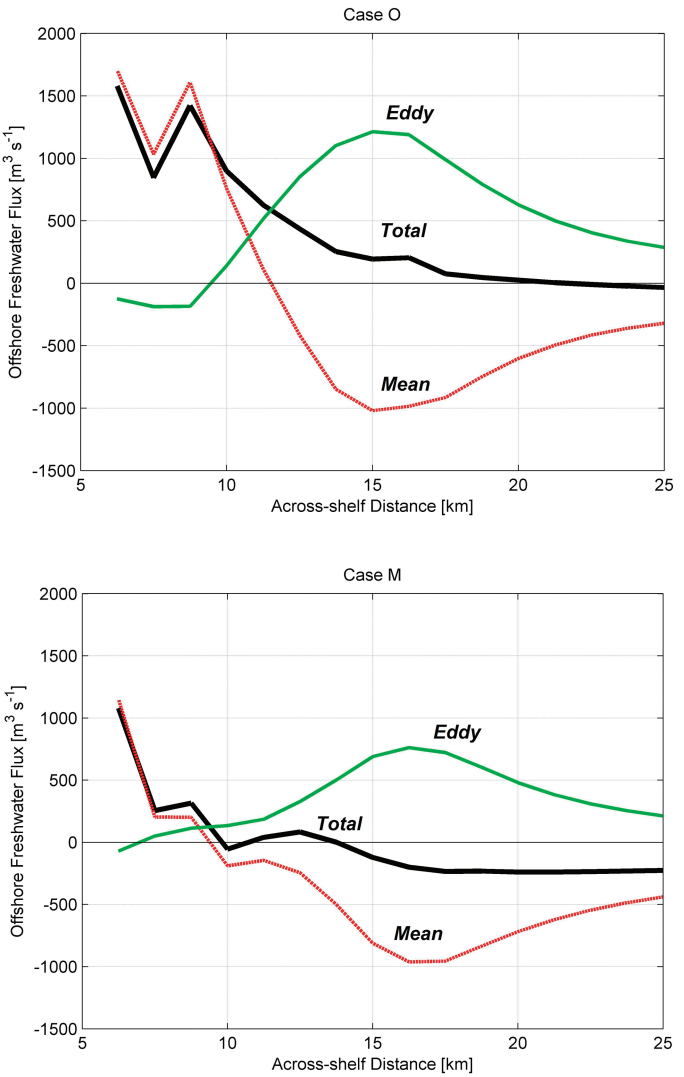

Figure 13. 30-day averaged across-shelf freshwater flux (positive offshore): total (thick black), mean (red), and eddy (green) for model case O (top) and M (bottom).

Thus, the total positive freshwater flux penetrates further offshore in Case O ($x \sim 17$ km) due to the eddy flux component.

Next, we analyze the spatial structure of the freshwater transport at $x = 15$ km, where in both model runs the corresponding mean and eddy transports reach their maximum magnitude. In Case M (Fig. 14), the total freshwater transport is onshore in the central part of the model domain (where the downwelling-favorable wind is at a maximum), while offshore transport occurs at the edges and occupies a relatively thin surface layer. The

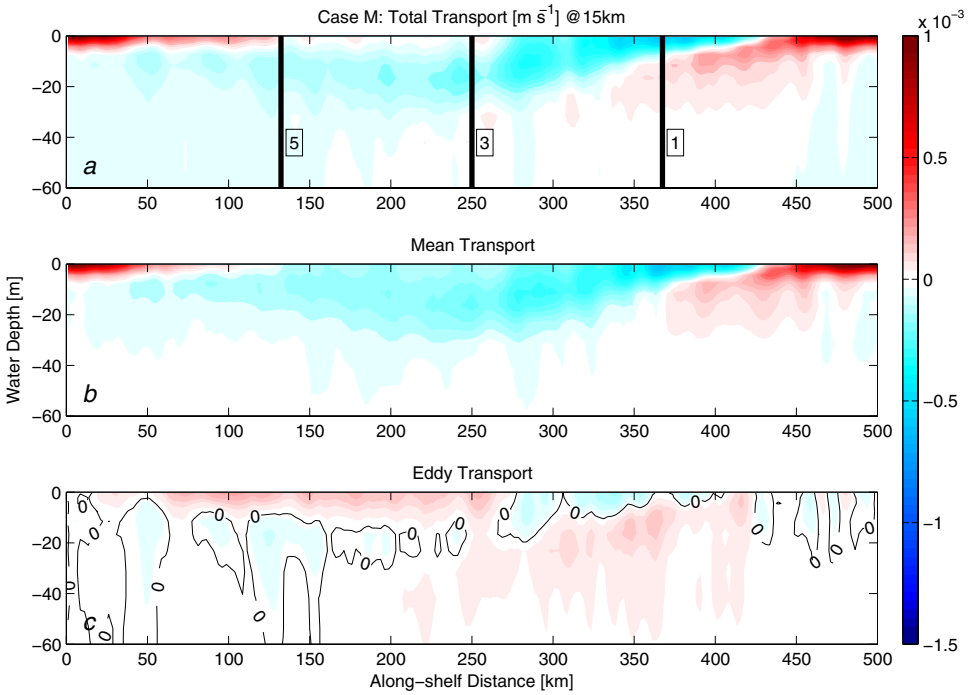

Figure 14. 30-day averaged across-shelf freshwater transport in model case M at $x = 15$ km: total (a), mean (b) and eddy (c).

onshore transport is determined primarily by its mean component (compare Fig. 14a and b), and is associated with the Ekman transport. The offshore mean freshwater transport develops in the areas where the winds subside and the buoyant plume is allowed to spread laterally. In the eddy component, positive and negative values are intermittent; however, positive (offshore) transport prevails. This is evident from a rather limited area of negative values encircled by the zero contour in Figure 14c, as well as from the integral eddy flux at this across-shelf location (Fig. 13). Eddy transport is consistently positive at the surface in the downstream half of the source region ($y = 60$–250 km). Here the wind stress converges (decreases in the downstream direction). Total transport in Case O (Fig. 15) is less spatially organized. The mean component is again largely negative (onshore), especially at the edges of the model domain where the wind stress now has a maximum magnitude. Within the source region there are several patches of positive freshwater transport which are associated with the bulging of a buoyant layer (this is also seen in the surface salinity field in Fig. 12d). Eddy transport is mostly positive in the upstream part of the source region ($y = 300$–450 km), and its absolute values are comparable with those of the mean transport. This offshore eddy-driven freshwater transport is both stronger and deeper (more than 40-m deep) than in Case M, but in both cases, as well as in other cases with the variable wind, it develops predominantly in the area of converging wind stress.

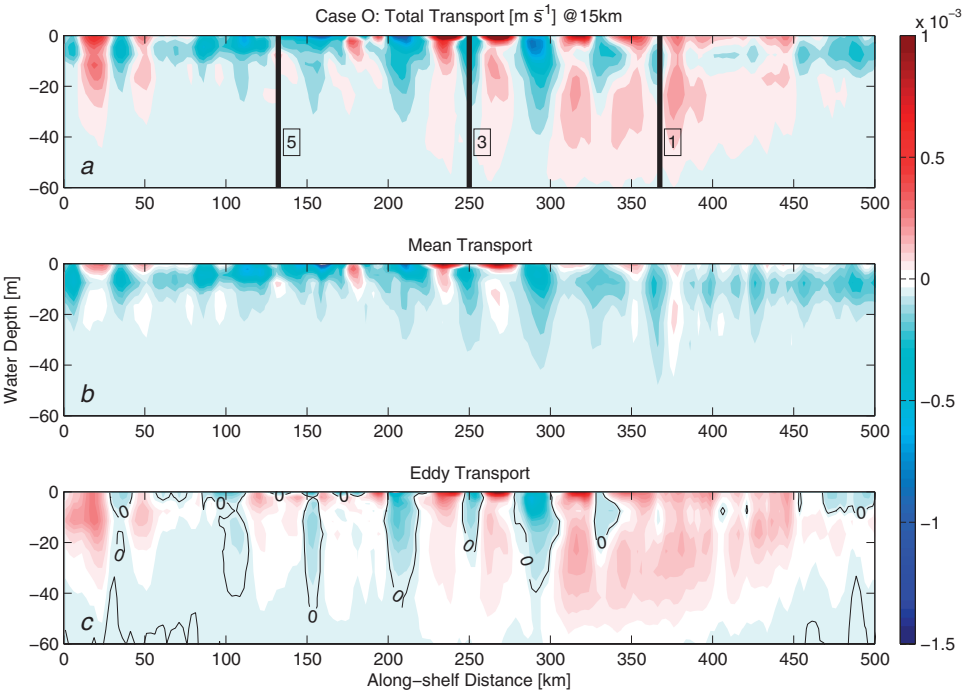

Figure 15. Same as Figure 14 but for model case O.

A final case considered here is when the wind stress reverses to upwelling-favorable in the source region (Case N). Although the upwelling wind stress was extremely light (a maximum of 0.002 Pa) and the along-shelf-averaged wind stress was zero, this wind forcing resulted in the second-lowest gain with significant offshore spreading of the buoyant layer within the source region (not shown). As upwelling-favorable wind further increased in the source region (these model runs are not included in this contribution), the downstream flux of freshwater was completely halted, the coastal current reversed to flow upstream, and the buoyant water spread offshore across the entire model domain.

4. Discussion

In this study, we modeled the impact of wind forcing and its spatial variations on the freshwater transport by a coastal buoyancy-driven current resembling a segment of the Alaska Coastal Current. The ACC extends over thousands of kilometers in the alongshore direction and does not have a readily identifiable origin; hence, at any location its dynamics are affected by the buoyancy-influenced flow coming from upstream. To mimic this feature of the ACC, we applied periodic boundary conditions, which allowed for the propagation of a naturally formed coastal current through the upstream boundary. With this configuration, the freshwater content in the coastal current monotonically grew through the duration

of each model experiment. This situation corresponds to the conditions in summer and early fall in the GOA region, when the freshwater discharge increases dramatically (Fig. 3). As a measure of the fate of freshwater discharge in the source region with multiple inflows, we calculated a gain in downstream freshwater flux between the upstream and downstream boundaries of the source region.

The gain turned out to be comparable for both no wind and moderate downwelling-favorable wind conditions. The continuous buoyancy driven current arrests the growth of the anticyclonic bulges that form near the mouth of the individual inflows and forces newly discharged freshwater downstream. Downwelling-favorable wind traps the buoyant layer closer to the coast (as compared to no wind conditions) but also enhances the across-shelf density gradient and corresponding geostrophic shear in the along-shelf current. This results in the development of rich mesoscale variability which spreads buoyant water offshore and reduces the freshwater flux gain through the source region. Because of this strong mesoscale variability, the downstream freshwater flux can fluctuate over several days with magnitudes comparable to the net freshwater discharge into the source region. These fluctuations necessitate using monthly-averages in calculating the freshwater flux gain.

The important finding here is that the gain is substantially reduced ($\sim$40% of the coastal freshwater discharge) under light and variable downwelling-favorable wind conditions. Such wind forcing is sufficient to deepen the buoyant layer and to enhance the vertical shear of along-shelf velocity through onshore Ekman transport. At the same time, the frictional effects under light wind are insignificant, and the actual velocity shear is close to geostrophic. The increase in wind stress magnitude increases the geostrophic shear but reduces the actual shear and consequently reduces the offshore eddy flux of freshwater. Alongshore variations of wind forcing further increase the offshore loss of freshwater. The maximum offshore transport of freshwater is associated with regions of converging wind (decreasing wind stress in downstream direction).

Alongshore wind variations affect the offshore transport of freshwater primarily through the eddy component, while its mean component is less affected. We found that the alongshore pressure gradient in Case O (lowest gain) at the surface was insignificant and could not contribute to the mean offshore transport. The alongshore pressure gradient was noticeable (but still weak) in Case M, where both wind and freshwater discharge built up a high pressure in the center of model domain. Even in this case, the alongshore pressure gradient at the surface could account for only $\sim$0.02 m s^{-1} offshore flow (assuming geostrophic balance) and decreased with depth.

Light and variable wind conditions prevail in the GOA region during the summer (Figures 2 and 3). Weingartner *et al.* (2005) analyzed the climatology of the ACC and found a surprising result: major characteristics of the ACC, such as the freshwater transport and the baroclinic component of the mass transport correlate well with the total freshwater discharge during most of the year except in summer, when the wind forcing subsides and

runoff increases. Results presented in this study can potentially explain an offshore loss of freshwater in the ACC system on monthly time scales under typical summer conditions.

Upwelling-favorable winds effectively block the downstream freshwater transport and spread the buoyant layer offshore. In this regard our results are consistent with numerous previous studies on the effects of upwelling-favorable wind on buoyant plume dynamics (e. g., Xing and Davis, 1999; Fong and Geyer, 2001; García Berdeal *et al.,* 2002). Multiple and relatively small sources of buoyant water seem to be more sensitive to upwelling wind conditions when compared to major single-source discharges, as both our simulations and recent observations along the South California Bight (Warrick *et al.,* 2007) indicate. However, upwelling events are less frequent in the GOA region than downwelling wind conditions.

5. Conclusion

Light downwelling-favorable winds, both uniform and spatially-variable, can adversely affect downstream freshwater transport in a coastal current driven by multiple freshwater sources over a long section of coastline. We quantified this effect in our study by computing the gain in downstream freshwater flux within the source region, which is a segment of an ACC-like coastal system. When the spatially averaged wind stress is $\sim$0.025 Pa or less, the gain is only 35–45% of the net freshwater discharge through the source region, while the rest of discharge spreads offshore rather than downstream. The gain was close to 60% under no wind or moderate wind ($\tau \sim 0.05$–0.1 Pa) conditions. The offshore freshwater transport is eddy-driven and is enhanced in the areas of converging wind forcing. Eddy generation is associated with the wind-induced deepening of the buoyant layer near the coast. When the turbulent friction is weak, this deepening enhances the vertical shear of the alongshore current through the thermal wind balance and promotes instability and an offshore eddy freshwater flux. Although motivated by observations in the GOA region, the results are applicable to other coastal systems driven by multiple or continuous sources of buoyant water.

Acknowledgments. J. R.-C. and A. Y. were partially supported by NSF grant SGER OCE-0650194. T. W. was supported by US GLOBEC Program (NSF-NOAA) under grant OCE-1019078 and by North Pacific Research Board Project # 708. The authors are indebted to Ken Brink and two anonymous reviewers for their insightful comments and suggestions. With this contribution we commemorate many years of friendship with Rich Garvine. Rich was always generous with his insights and assistance, which helped us grow as marine scientists. More importantly, his humility, faith and kindness still dwell with us and make us better humans.

REFERENCES

Bacon, S., G. Reverdin, I. G. Rigor, and H. M. Snaith. 2002. A freshwater jet on the east Greenland shelf. J. Geophys. Res., *107*(C7), doi:10.1029/2001JC000935.

Blanton, J. O. and L. P. Atkinson. 1983. Transport and fate of river discharge on the continental shelf of the southeastern United States. J. Geophys. Res., *88,* 4730–4738.

Fong, D. A. and W. R. Geyer. 2001. Response of a river plume during an upwelling favorable wind event. J. Geophys. Res., *106,* 1067–1084.

—— 2002. The alongshore transport of freshwater in a surface-trapped river plume. J. Phys. Oceanogr., *32,* 957–972.

Fong, D. A., W. R. Geyer and R. P. Signell. 1997. The wind-forced response of a buoyant coastal current: Observations of the western Gulf of Maine plume. J. Mar. Syst., *12,* 69–81.

García Berdeal, I., B. M. Hickey and M. Kawase. 2002. Influence of wind stress and ambient flow on a high discharge river plume. J. Geophys. Res., *107*(C9), doi:10.1029/2001JC000932.

Garvine, R. W. 1995. A dynamical system for classifying buoyant coastal discharges. Cont. Shelf Res., *15,* 1585–1596.

Gill, A. E. 1982. Atmosphere-Ocean Dynamics, Academic Press, 662 pp.

Hermann, A. J. and P. J. Stabeno. 1996. An eddy-resolving model of circulation on the western Gulf of Alaska shelf. 1. Model development and the sensitivity analysis. J. Geophys. Res., *101,* 1129–1149.

Horner-Devine, A. R., D. A. Fong, S. G. Monismith, and T. Maxworthy. 2006. Laboratory experiments simulating a coastal river inflow. J. Fluid Mech., *555,* 203–232.

Large, W. G., J. C. McWilliams, and S. C. Doney. 1994. Oceanic vertical mixing: A review and a model with a nonlocal boundary layer parameterization. Rev. Geophys., *32,* 363–403.

Lentz, S. J. and K. R. Helfrich. 2002. Buoyant gravity currents along a sloping bottom in a rotating fluid. J. Fluid Mech., *464,* 251–278.

Mork, M. 1981. Circulation phenomena and frontal dynamics of the Norwegian Coastal Current. Phil. Trans. R. Soc. Lond., *A 302,* 635–647.

Narayanan, C. and R. W. Garvine. 2002. Large scale buoyancy driven circulation on the continental shelf. Dyn. Atmos. Oceans, *36,* 125–152.

Nof, D., and T. Pichevin. 2001. The Ballooning of Outflows. J. Phys. Oceanogr., *31,* 3045–3058.

Royer, T. C. 1982. Coastal freshwater discharge in the Northeast Pacific. J. Geophys. Res., *87,* 2017–2021.

Schumacher, J. D., C. A. Pearson and J. E. Overland. 1982. On exchange of water between the Gulf of Alaska and the Bering Sea through Unimak Pass, Alaska. J. Geophys. Res., 87, 5785–5795.

Shchepetkin, A. F. and J. C. McWilliams. 2005. The regional oceanic modeling system (ROMS): a split-explicit, free-surface, topography-following-coordinate oceanic model. Ocean Mod., *9,* 347–404.

Song, Y. and D. Haidvogel. 1994. A semi-implicit ocean circulation model using a generalized topography-following coordinate system. J. Comput. Phys., *115,* 228–244.

Spall, M. A. and D. C. Chapman. 1998. On the efficiency of baroclinic eddy heat transport across narrow fronts. J. Phys. Oceanogr., *28,* 2275–2287.

Stabeno, P. J., N. A. Bond, A. J. Hermann, N. B. Kachel, C. W. Mordy, and J. E. Overland. 2004. Meteorology and oceanography of the Northern Gulf of Alaska. Cont. Shelf Res., *24,* 859–897.

Stabeno, P. J. and A. J. Hermann. 1996. An eddy-resolving model of circulation on the western Gulf of Alaska shelf. 2. Comparison of results to oceanographic observations. J. Geophys. Res., *101,* 1151–1161.

Warrick, J. A., P. M. DiGiacomo, S. B. Weisberg, N. P. Nezlin, M. Mengel, B. H. Jones, J. C. Ohlmann, L. Washburn, E. J. Terrill and K. L. Farnsworth. 2007. River plume patterns and dynamics within the Southern California Bight. Cont. Shelf Res., *27,* 2427–2448.

Weingartner, T. J., S. L. Danielson, and T. C. Royer. 2005. Freshwater variability and predictability in the Alaska Coastal Current. Deep-Sea Res. II, *52,* 169–191.

Whitney, M. M. and R. W. Garvine. 2005. Wind Influence on a coastal buoyant outflow. J. Geophy. Res., *110,* C03014, doi:10.1029/2003JC002261.

Williams, W. J., T. J. Weingartner and A. J. Hermann. 2007. Idealized three-dimensional modeling

of seasonal variation in the Alaska Coastal Current. J. Geophys. Res., *112,* C07001, doi:10.1029/2005JC003285.

Xing, J. and A. M. Davies. 1999. The effects of wind direction and mixing upon the spreading of a buoyant plume in a non-tidal regime. Cont. Shelf Res., *19,* 1437–1487.

Yankovsky, A. E. 2000. The cyclonic turning and propagation of buoyant coastal discharge along the shelf. J. Mar. Res., *58,* 585–607.

Yankovsky, A. E. and D. C. Chapman. 1997. A simple theory for the fate of buoyant coastal discharges. J. Phys. Oceanogr., *27,* 1386–1401

Received: *7 April, 2008;* revised: *4 December, 2008.*